



Prediction of the Elastic Properties of a Plain Woven Carbon Fiber Reinforced Composite with Internal Geometric Variability

Chao Zhu^{1,2} · Ping Zhu^{1,2} · Zhao Liu^{1,2} · Wei Tao^{1,2} · Wei Chen^{1,3}

Received: 1 September 2017 / Accepted: 6 January 2018 / Published online: 20 June 2018
© Society of Automotive Engineers of China (SAE-China) 2018

Abstract

A statistical analysis of the yarn parameters of a plain woven carbon fiber reinforced polymer composite was conducted using X-ray micro-computed tomography data. An algorithm based on the correlated Gaussian random sequence was proposed to construct statistically equivalent yarns, which were introduced into a numerical multiscale model. A representative volume element was created to evaluate the macroscopic elastic properties of the composite. The predicted elastic constants showed a good agreement with experimental data obtained from tensile, compressive, and shear tests. This showed the importance of considering internal geometric variability for obtaining accurate simulation results. Finally, the performance of an electric vehicle back door made of the composite material was calculated by finite element analysis. The weight of the back door system was reduced by 47.45%, and performance results showed an excellent prospect of using lightweight composites.

Keywords Plain woven CFRP · X-ray micro-CT · Statistical reconstruction · Multiscale modeling · CFRP back door

Abbreviations

Micro-CT	Micro-computed tomography
CGRS	Correlated Gaussian random sequence
RVE	Representative volume element
CFRP	Carbon fiber reinforced polymer
VIP	Vacuum infusion process
A	Area
AR	Aspect ratio
PBC	Periodic boundary conditions
SMC	Sheet molding compound
UMAT	User-defined material
CAD	Computer aided design
CAE	Computer aided engineering

1 Introduction

To address issues of environmental pollution and resource consumption, lightweight vehicles fulfill stringent fuel efficiency requirements for both conventional and electric cars while maintaining safety and performance. Use of novel materials is an important aspect of lightweight design. CFRP has been increasingly employed in the automobile industry [1,2] because they are lightweight but have high specific stiffness and strength [3,4]. To explore the performance of automotive parts made of CFRP, numerical studies including multiscale modeling of its mechanical properties have been performed [5,6].

The internal geometric variability of a woven fiber reinforced polymer cannot be ignored because it has a nonnegligible effect on the mechanical properties such as the elastic constants [7]. There are inevitable fluctuations in the internal geometric structure of the yarns used to manufacture textile reinforced polymer composites. For example, the microstructures in plain or satin woven CFRP are grid-like, in which weft yarn goes over and under warp yarn. Combined with the molding process, the yarn shape and path possess spatial variability. Internal structure variability is directly related to the macroscopic properties of composites [8,9]. Lee et al. [10] investigated the elastic properties of plain woven fabric reinforced aluminum matrix composites through combined

✉ Ping Zhu
pzhu@sjtu.edu.cn

¹ State Key Laboratory of Mechanical System and Vibration, School of Mechanical Engineering, Shanghai Jiao Tong University, Shanghai 200240, People's Republic of China

² Shanghai Key Laboratory of Digital Manufacture for Thin-Walled Structures, School of Mechanical Engineering, Shanghai Jiao Tong University, Shanghai 200240, People's Republic of China

³ Department of Mechanical Engineering, Northwestern University, 2145 Sheridan RD Tech B224, Evanston, IL 60201, USA

analytic and experimental methods and concluded that the variability of reinforcement geometric parameters such as shape of the yarn section and gap length had some degree of influence on elastic constants. Endruweit et al. [11] studied the influence of fiber angle variations on the permeability of textile fabrics via stochastic injection simulations in which the variability of reinforcement was emphasized. De Carvalho et al. [12] conducted four-point bending and compact compression experiments on two-dimensional (2D) woven composites and stated that the location and morphology of the damage initiation depended on the weave architecture and internal geometry. Goldsmith et al. [13] characterized statistical distributions of architecture parameters of satin weave composites from cross section micrographs, and relationships between these parameters and the thermo-mechanical properties were constructed via a response surface method. They found that tow width, tow spacing, and volume fractions affected the variability in the mechanical properties. Olave et al. [14] employed multiscale modeling and sensitivity analysis to determine the influence of geometric variability of woven composites on their stiffness and concluded that laminate thickness and orientation contributed to the stiffness dispersion.

As the internal geometric architecture of woven composites influences the elastic properties, it is essential to characterize the geometric parameters as accurately as possible while analyzing the behaviors of composites under realistic loading conditions. Optical methods coupled with statistical analysis have been adopted to study the internal geometric variability in recent years. Desplentere et al. [15] explored the use of X-ray micro-CT and optical micrographs to measure stochastic geometric parameters of textile composites, and found that there was no significant differences between the two techniques. Barbero et al. [16] used photomicrographs of sectioned plain woven laminates to measure their internal geometry, from which accurate finite element RVE models were built to predict elastic properties. Internal shape and positions of yarns including yarn centroids, area, and AR of cross sections in three-dimensional (3D) woven composites were analyzed statistically by micro-CT [17]. Vanaerschot et al. [18] employed similar methods to describe stochastic internal geometric parameters of a twill woven carbon-epoxy composite. Blacklock et al. [19] proposed the Monte Carlo Markov Chain algorithm to generate stochastic replicas of textile composites that were statistically equivalent to the specimens imaged via high-resolution computed tomography. Rinaldi et al. [20] used a similar algorithm to construct solid 3D tow representations of textile composites. Topological rules were defined to resolve interpenetrations or disorders among tows, and the shape and smoothness were adjusted using a geometric rule.

The aim of this research was to predict the elastic properties of plain woven CFRP by statistically analyzing

the internal geometric variability and reconstructing a statistically equivalent RVE. First, the internal geometric parameters of plain woven CFRP were acquired by micro-CT experiments and statistically analyzed. Second, the architecture of an RVE was reconstructed with the CGRS method, from which a finite element model was established for the prediction of elastic properties. Finally, the performance of a back door of an electric vehicle made of plain woven CFRP was calculated, illustrating the effect of using this lightweight material.

2 Experimental Measurements and Statistical Analysis

To obtain the geometric characteristics of the plain woven CFRP, 3D micro-CT scanning was conducted. For these measurements, no processing of the prepared sample was required. Based on the 3D volume image, the geometric parameters of the yarns were extracted in sections and then statistical analysis was performed to determine the mean trend and the correlated deviations, which served as the basis of further reconstruction.

2.1 Material and Experiment Preparation

A plain woven CFRP composite with a nominal unit cell dimension of 4 mm × 4 mm was considered in this study. The sample material system consisted of a matrix of epoxy resin (provided by Huntsman[®] Corporation) and TC33 carbon fiber (manufactured by Tairafil[®]). The composite was fabricated in a plain woven manner with 3000 carbon fibers contained inside one yarn of the plain woven fabric. The plain woven fabric was infiltrated by the epoxy resin matrix, and the laminated plate was manufactured using a VIP. Once the plate was cut to the required size, no additional treatment was needed for micro-CT analysis.

To obtain enough information for statistical analysis, images of at least one period length range in two principal directions of several plies were needed. Additionally, the X-ray micro-CT scanning requires a smaller sample size to achieve higher resolution. The length, width, and thickness of the samples used in this research were 5.8, 5.0, and 4.8 mm, respectively. X-ray absorption contrast between the carbon fiber yarns and epoxy resin is low; therefore, the voltage and current of the X-ray beamline and the technical parameters of the micro-CT equipment were adjusted according to the specific absorption characteristics of material [21].

2.2 Geometry Variability Measurement

The internal structure of the composite was acquired by X-ray micro-CT. The sample was scanned in SkyScan 1272

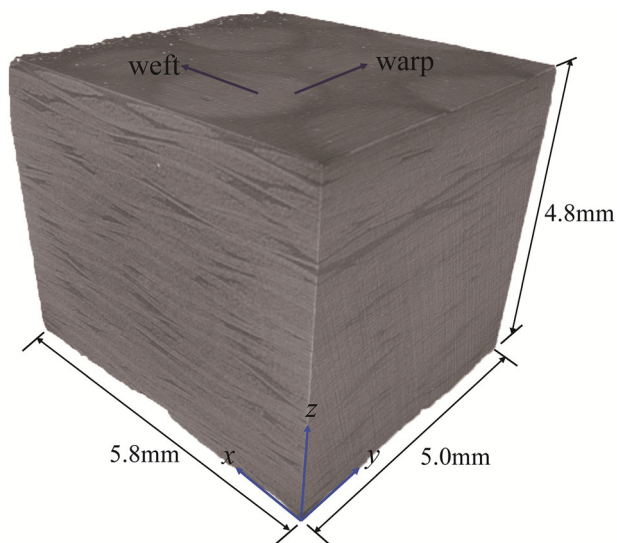


Fig. 1 3D micro-CT image of the plain woven CFRP

(manufactured by Bruker[®] Corporation) with a voxel resolution of 7.8 μm at a voltage of 50 kV and current of 200 μA. The 3D volume representation of the sample from the micro-CT scan is shown in Fig. 1. A processed 2D cross-sectional image is illustrated in Fig. 2. While there are areas in which it is hard to distinguish yarn from matrix, the images were clear enough to determine the yarn parameters.

A series of cross-sectional images uniformly distributed in both the warp and weft directions were acquired at the scale of a complete RVE to analyze the geometric properties of the yarns. The material was divided into twenty equally spaced parts, i.e., twenty-one slices were analyzed in both directions, and the images were segmented and labeled manually.

The cross sections of the yarns were approximately elliptical [7]. To acquire the yarn characteristics, the yarn cross sections were fitted into an ellipses and geometric data were recorded using the Java-based image processing freeware ImageJ. The shape fitting operation yielded the coordinates of its centroid (x, y, z), the yarn area A, the AR, and the orientation θ of the yarn cross section along the entire yarn path, as shown in Fig. 2.

2.3 Statistical Characterization

Because of the internal structure symmetry of plain woven composites, geometric variability was assumed to be identical in the warp and weft directions. Thus, the warp and weft yarns were classified into one genus that can be statistically analyzed in the same way. Taking the warp direction as the y-axis, the obtained yarn structure dataset is presented by (x_nⁱ, z_nⁱ, AR_nⁱ, A_nⁱ, θ_nⁱ), in which n = 1, . . . , 21 is the slice number and i represents the warp yarn number. The analysis of statistical parameters was similar to the statistical method

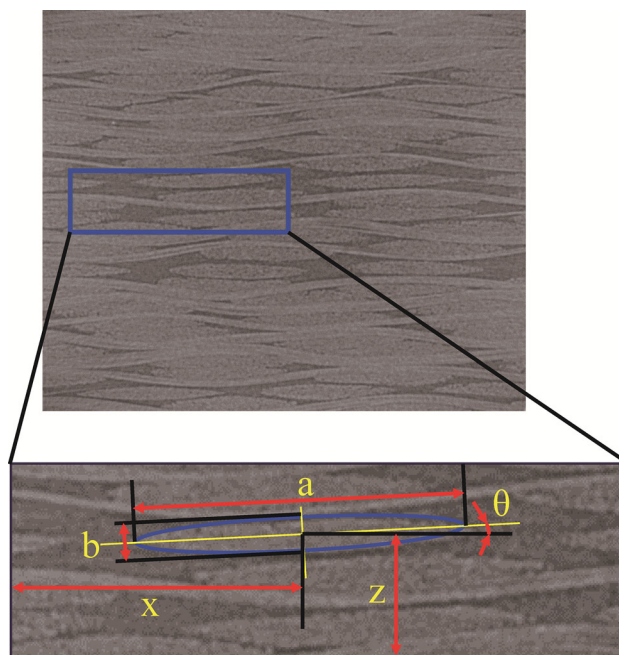


Fig. 2 Geometric parameters of the fitted yarn cross sections

proposed by Bale [10] and Vanaerschot et al. [11]. Each yarn structural parameter is expressed as the sum of the mean and stochastic parameters:

$$\varepsilon_n^i = \langle \varepsilon_n^i \rangle + \delta_n^i \tag{1}$$

where ε denotes one of the defined parameters, ⟨ε_nⁱ⟩ is the systematic mean value at location n of yarn i, and δ_nⁱ is the zero-mean deviation.

Six warps were used to obtain the statistical parameters. The global mean parameter values are listed in Table 1, and Figure 3 shows the systematic trends of the warp yarn path and geometric parameters of the warp yarns. The x and θ trends seemed to be random along the warp directions, while the variation of z was characterized by a cosine curve with reciprocal trough and crest in one reference period range. The systematic trends of AR and A demonstrated two cycles in nearly the same distance with reciprocal crests and valleys in one period length, which is because warp and weft yarns are compressed with each other, especially at crossover locations. The patterns of systematic trends of z, AR, and A could also imply that information extracted from six warp yarns is sufficient for this material to some extent. The global mean values of the yarn parameters defined above are listed in Table 1.

The deviations from the systematic mean trend at each location were extracted by subtracting the calculated systematic values. The cumulative probability density functions of the normalized deviations for all five warp yarn parameters are illustrated in Fig. 4a. Figure 4b demonstrates the normal

Table 1 Global mean values and standard deviations of yarn parameters

	x (mm)	z (mm)	AR	A (mm ²)	θ (°)
Mean	0.983	0.150	10.960	0.163	1.583
Standard deviation	0.092	0.057	1.398	0.017	0.882

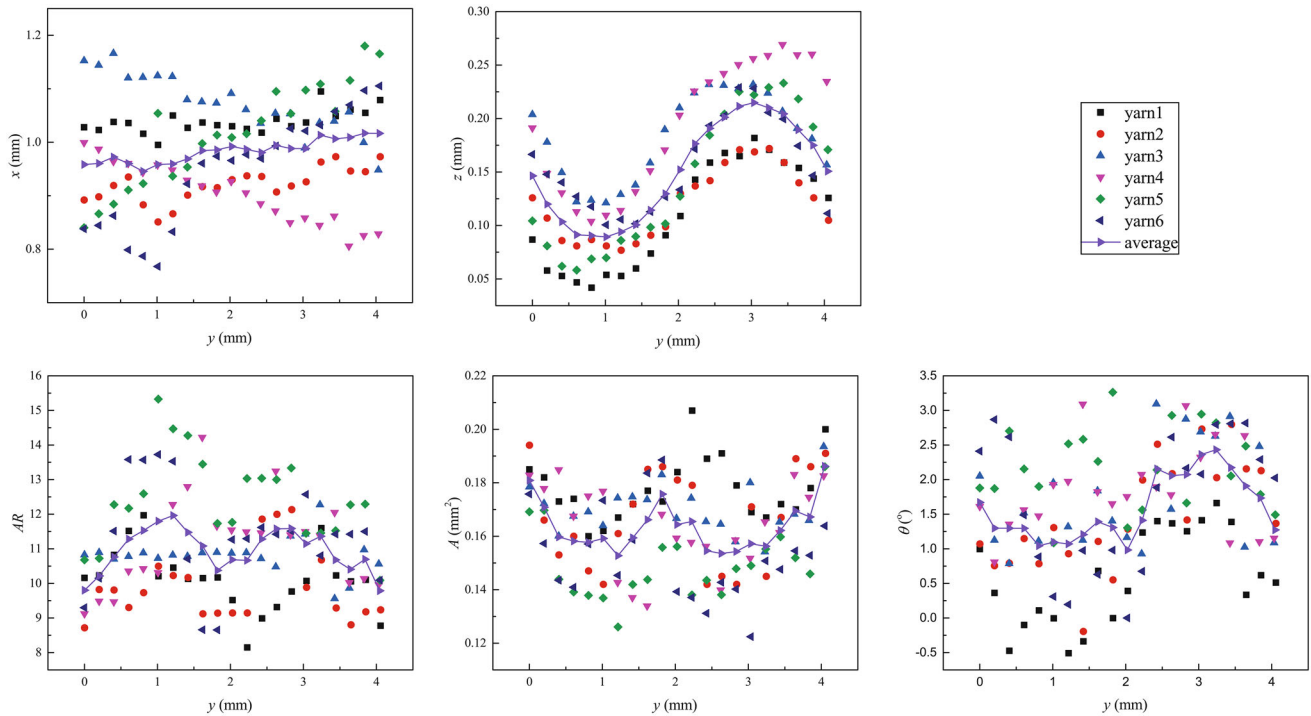


Fig. 3 The systematic values of the warp yarn geometric parameters in one reference period

probability plots of each normalized deviation. The deviations of the five parameters had an approximately normal distribution over most of the variable range.

The standard deviation of each parameter was computed by:

$$\sigma_\varepsilon = \sqrt{\frac{\sum_{n,i} (\delta_n^i)^2}{N - 1}} \tag{2}$$

where $N = \sum_n N_n$ and N_n is the number of data points at grid location n . The standard deviations of each parameter are shown in Table 1.

The autocorrelation coefficient of a parameter δ^i is calculated by:

$$C_{\text{auto}}^i(k) = \frac{\sum_{n=1}^{m-k} \delta_n^i \delta_{n+k}^i}{\sqrt{\sum_{n=1}^{m-k} (\delta_n^i)^2} \sqrt{\sum_{n=1}^{m-k} (\delta_{n+k}^i)^2}} \tag{3}$$

where $(\delta_n^i, \delta_{n+k}^i)$ is a pair of data points taken from two different locations along the same yarn, m is the number of pairs, and k is an integer. The Pearson’s correlation parameter was utilized to summarize the autocorrelations of geometric

parameters based on the entire warp yarn genus dataset. The autocorrelation graphs of geometric parameters (take x and AR as examples) are illustrated in Fig. 5.

3 Geometric Modeling of RVE

Once the statistical characteristics of the defined geometric parameters were acquired, an RVE with identical statistical information as measured in the material sample was generated. The main goal was to reconstruct a sequence of random deviations at certain grid locations along the yarn path that accommodated the correlation relationship among points at different distances.

3.1 Development of Reconstruction Algorithm

An algorithm based on CGRS was developed to reconstruct the deviations of yarn feature parameters in woven composites. An assumption of normal distribution of the deviation for each geometric parameter was made based on the cumulative distribution functions and normal probability plots

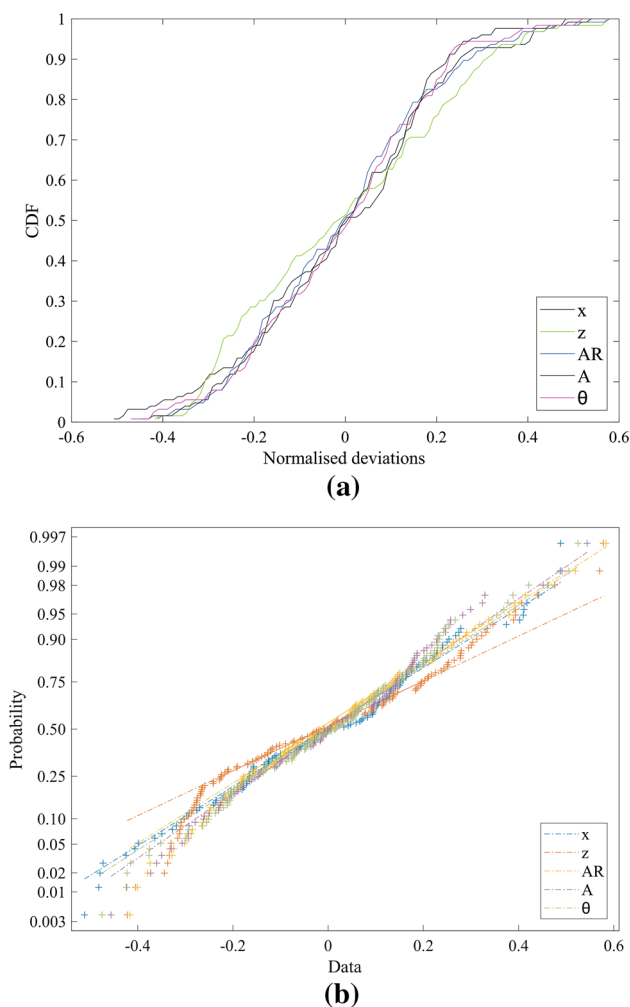


Fig. 4 **a** Cumulative distribution functions and **b** normal probability plots of the normalized deviations of the five warp yarn parameters

shown in Fig. 4. The joint probability density function of the N -dimensional normal vector $\mathbf{X} = [X_1, X_2, \dots, X_N]^T$ is:

$$f_{\mathbf{X}}(x_1, \dots, x_N) = \frac{1}{(2\pi)^{N/2} |\mathbf{K}|^{1/2}} \exp\left\{-\frac{1}{2}(\mathbf{x} - \boldsymbol{\mu})^T \mathbf{K}^{-1}(\mathbf{x} - \boldsymbol{\mu})\right\} \quad (4)$$

where $\mathbf{x} = [x_1, \dots, x_N]^T$ and $\boldsymbol{\mu} = [\mu_1, \dots, \mu_N]^T$ is the mean vector of \mathbf{X} . The covariance matrix \mathbf{K} is related to the correlation information of \mathbf{X} , which is symmetric positive definite and expressed as:

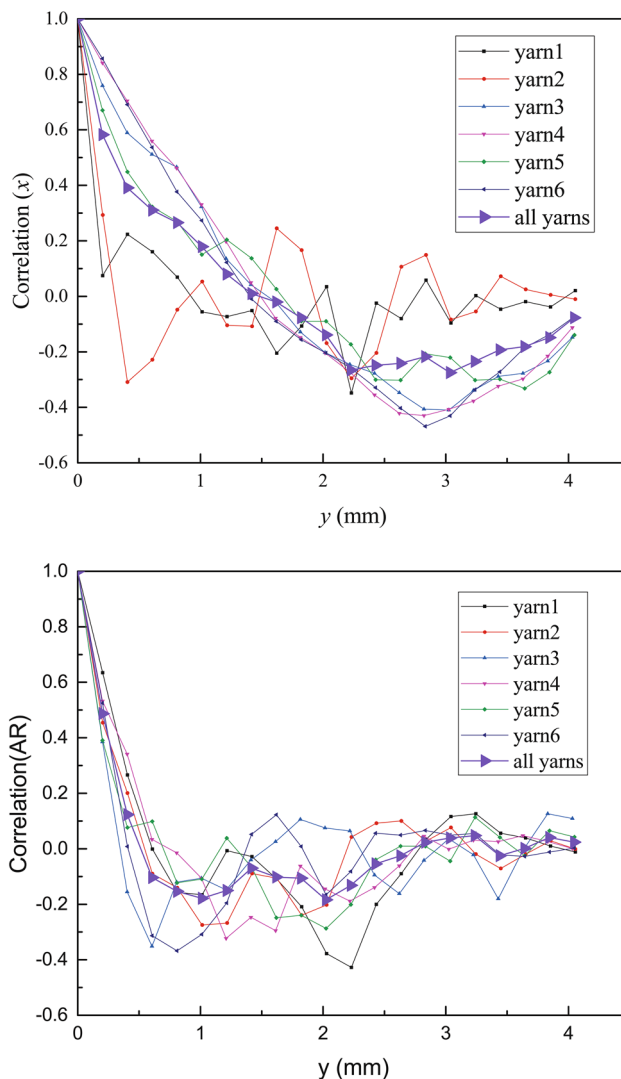


Fig. 5 Autocorrelation graphs of the warp yarn geometric parameters

$$\mathbf{K} = \begin{bmatrix} k_{11} & k_{12} & \dots & k_{1N} \\ k_{21} & k_{22} & \dots & k_{2N} \\ \vdots & \vdots & \dots & \vdots \\ k_{N1} & k_{N2} & \dots & k_{NN} \end{bmatrix} = \begin{bmatrix} R_X(0) & R_X(1) & \dots & R_X(N-1) \\ R_X(1) & R_X(0) & \dots & R_X(N-2) \\ \vdots & \vdots & \ddots & \vdots \\ R_X(N-1) & R_X(N-2) & \dots & R_X(0) \end{bmatrix} \quad (5)$$

in which $R_X(m)$ is the covariance function of \mathbf{X} . In this research, an exponential function was adopted to fit the autocorrelation graph of Fig. 5 to determine the standard autocorrelation function.

$$R_X(m) = \sigma^2 \exp(-\alpha m), \alpha > 0 \quad (6)$$

The correlated normal random vector \mathbf{X} was transformed from a standard normal random vector \mathbf{U} using the relationship:

$$\mathbf{X} = \mathbf{AU} + \boldsymbol{\mu} \quad (7)$$

The symmetric positive definite correlation matrix \mathbf{K} was decomposed as the product of a lower triangular matrix and its transposed matrix according to matrix theory:

$$\mathbf{K} = \mathbf{AA}^T \quad (8)$$

$$\mathbf{A} = \begin{bmatrix} a_{11} & 0 & \cdots & 0 \\ a_{21} & a_{22} & \cdots & 0 \\ \vdots & \vdots & \cdots & \vdots \\ a_{N1} & a_{N2} & \cdots & a_{NN} \end{bmatrix} \quad (9)$$

Then, the issue was transformed to identify the components of the matrix \mathbf{A} . The entries of \mathbf{A} could be calculated sequentially by column. For the first column, the components could be computed as:

$$a_{11} = \sqrt{k_{11}}, \quad a_{i1} = k_{i1}/a_{11} \quad (10)$$

Once the $j - 1$ columns were determined, then the diagonal element of column j could be calculated:

$$a_{jj} = \left[k_{jj} - \sum_{k=1}^{j-1} a_{jk}^2 \right]^{1/2} \quad (11)$$

The entries under the diagonal line were determined by:

$$a_{ij} = a_{jj}^{-1} \left[k_{ij} - \sum_{k=1}^{j-1} a_{ik}a_{jk} \right], \quad i = j + 1, \dots, N \quad (j < N) \quad (12)$$

Using the calculation procedure detailed above, correlated deviations of each parameter with the same statistical features were reconstructed. The complete descriptive geometric parameters were then determined by adding the generated deviations onto the systematic values. The geometry information was further taken as parameters to build the RVE of a plain woven composite at the mesoscale.

3.2 Geometric Modeling

The reconstructed geometric parameters $(\mathbf{x}, z, \mathbf{AR}, \mathbf{A}, \boldsymbol{\theta})$ were used to build a series of elliptic cross sections along the warp direction in commercial CAD software such as CATIA (Dassault) and UG NX (Siemens). Continuous solid yarn geometry was then established based on these ellipses by lofting. Interpenetration between yarns was inevitable for each

yarn that was generated by the algorithm without considering positions relative to the other yarns. An intersecting operation was adopted to remove the interpenetration between yarns. Once the yarns were created, the matrix was represented as a cuboid space with the yarns within it. An example of an RVE is shown in Fig. 6a. As to be pointed out, small-scale wrinkles generally come from the geometry modeling method, alternative operations such as fitting yarn path using spline or setting more slices could be utilized to obtain more smooth surfaces.

4 Prediction of Elastic Properties

Based on geometric modeling of the RVE and the homogenization method, the elastic properties of the plain woven CFRP were calculated with the finite element method.

4.1 Finite Element Modeling

The RVE model was imported into finite element preprocessor Hypermesh (integrated in Altair® HyperWorks® software suite) and meshed using tetrahedral elements, which can be used to easily mesh complex geometric characteristics, as illustrated in Fig. 6b. The unit cell homogenization method was adopted to compute a homogeneous medium equivalent to the macroscopic heterogeneous composite in order to calculate the elastic properties of the plain woven CFRP. The effective stress and strain tensors, denoted as σ^* and ε^* , respectively, were calculated by volume averaging over the RVE and are described as:

$$\sigma^* = \frac{1}{V} \int_V \sigma(\mathbf{x})dV, \quad \varepsilon^* = \frac{1}{V} \int_V \varepsilon(\mathbf{x})dV \quad (13)$$

where V is the RVE volume.

The periodic characteristics of a composite are fulfilled when using a homogeneous RVE, thus, unified PBC were adopted [22]:

$$\begin{aligned} \vec{u}(0, x_2, x_3) - \vec{u}(L_1, x_2, x_3) &= \vec{U}_1 \\ \vec{u}(x_1, 0, x_3) - \vec{u}(x_1, L_2, x_3) &= \vec{U}_2 \\ \vec{u}(x_1, x_2, 0) - \vec{u}(x_1, x_2, L_3) &= \vec{U}_3 \end{aligned} \quad (14)$$

\vec{U}_1, \vec{U}_2 , and \vec{U}_3 are displacement vectors of the opposite faces, and L_1, L_2 , and L_3 denote the lengths of the RVE along three orthogonal directions. PBC defined in terms of displacements satisfy both the displacement periodicity and traction periodicity under the displacement-based finite element simulation framework.

The unified PBC was enforced by applying a linear equation constraint of corresponding nodes on a parallel opposite pair of faces in the finite element software Abaqus. As the nodes on edges or vertices belonged to more than one sur-

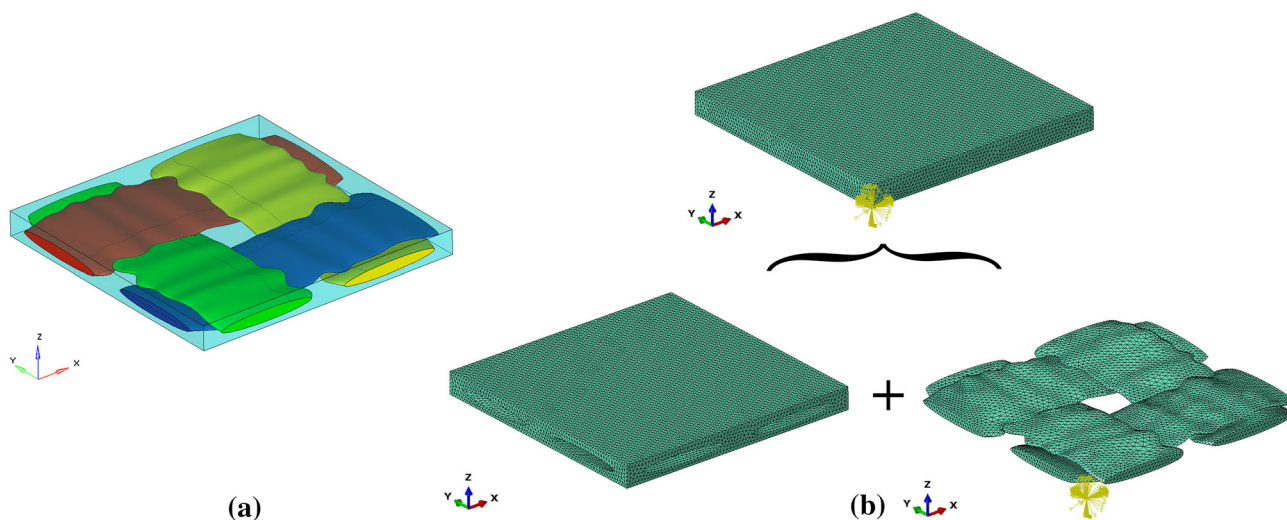


Fig. 6 a RVE geometric model and b RVE finite element model

Table 2 Mechanical properties of yarn and matrix

	Axial tensile modulus (GPa)	Axial compressive modulus (GPa)	Transverse modulus (GPa)	Major Poisson's ratio	Transverse Poisson's ratio	In-plane shear modulus (GPa)
Yarn	145.25	67.88	9.27	0.269	0.386	3.8
Matrix	3.08			0.35		

face, the constraint equations were merged into independent ones.

The macroscopic strain was calculated as:

$$\epsilon_{ii}^* = \frac{\bar{U}_i}{L_i}, \epsilon_{ij}^* = \frac{\bar{U}_i}{L_j}, (i \neq j) \tag{15}$$

where the subscript *i* denotes the direction of displacement loading. The macroscopic stress was calculated as:

$$\sigma_{ij}^* = \frac{(P_i)_j}{S_j} \text{ (no summation over } j) \tag{16}$$

where *S_j* denotes the area of the *j*th boundary surface on which the displacement was applied and $(P_i)_j$ is the traction force on the loading surface. Thus, the overall elastic response of the composite in terms of Young's modulus, Poisson's ratio, and shear modulus was calculated as:

$$E_{ii} = \frac{\sigma_{ii}^*}{\epsilon_{ii}^*}, \nu_{ij} = -\frac{\epsilon_{jj}^*}{\epsilon_{ii}^*}, G_{ij} = \frac{\sigma_{ij}^*}{\epsilon_{ij}^*} \tag{17}$$

The yarn possessed typical tensile-compressive asymmetry and was transversely isotropic, which is mainly due to the mechanical properties of the carbon fibers inside the yarn. The stress-strain relationship in the elastic range was described as:

$$\begin{pmatrix} \epsilon_{11} \\ \epsilon_{22} \\ \epsilon_{33} \\ \gamma_{12} \\ \gamma_{13} \\ \gamma_{23} \end{pmatrix} = \begin{pmatrix} \frac{1}{E_1} & -\frac{\nu_{12}}{E_1} & -\frac{\nu_{13}}{E_1} & 0 & 0 & 0 \\ -\frac{\nu_{12}}{E_1} & \frac{1}{E_2} & -\frac{\nu_{23}}{E_2} & 0 & 0 & 0 \\ -\frac{\nu_{13}}{E_1} & -\frac{\nu_{23}}{E_2} & \frac{1}{E_3} & 0 & 0 & 0 \\ 0 & 0 & 0 & \frac{1}{G_{12}} & 0 & 0 \\ 0 & 0 & 0 & 0 & \frac{1}{G_{13}} & 0 \\ 0 & 0 & 0 & 0 & 0 & \frac{1}{G_{23}} \end{pmatrix} \begin{pmatrix} \sigma_{11} \\ \sigma_{22} \\ \sigma_{33} \\ \tau_{12} \\ \tau_{13} \\ \tau_{23} \end{pmatrix} \tag{18}$$

Considering the tensile-compressive asymmetry, the elastic modulus in the axial direction was chosen as:

$$\begin{cases} E_1 = E_1^+ & \text{if } \sigma_1 \geq 0 \\ E_1 = E_1^- & \text{if } \sigma_1 < 0 \end{cases} \tag{19}$$

in which E_1^+ is the tensile axial elastic modulus and E_1^- is the compressive axial elastic modulus. Considering the transversely isotropic characteristics of the yarn, the elastic constants satisfied the equality constraints as:

$$\begin{aligned} E_2 &= E_3 \\ \nu_{12} &= \nu_{13} \\ G_{12} &= G_{13} \\ G_{23} &= \frac{E_2}{2(1 + \nu_{23})} \end{aligned} \tag{20}$$

The yarn properties were implemented in Abaqus with a UMAT. The elastic constants are shown in Table 2. The elas-

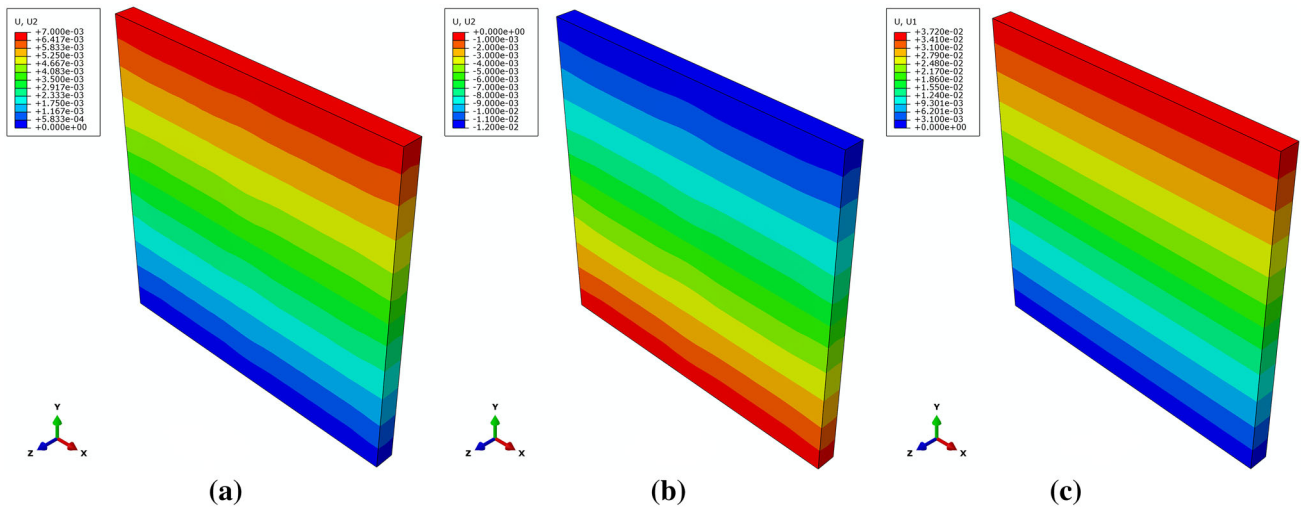


Fig. 7 Deformation contours of RVE under different loading conditions **a** tension, **b** compression, and **c** shear

Table 3 Predicted mechanical properties and experimental values

Properties	Axial tensile modulus (GPa)	Axial compressive modulus (GPa)	In-plane shear modulus (GPa)
Predicted values	59.21	24.54	3.50
Experimental values	60.89	24.09	3.63
Relative error (%)	2.76	-1.87	3.58

tic properties of the isotropic epoxy matrix are also listed in Table 2. Beyond the elastic range, the failure properties could be numerically predicted if the corresponding damage and failure criteria of constituents were defined, which will be presented in further research work.

4.2 Predicted Results

The elastic responses of the RVE model subjected to tensile, compressive, and shearing loads were simulated in ABAQUS/Standard. Deformation contours under different loading conditions are illustrated in Fig. 7. The tensile, compressive, and shear moduli were calculated, and the predicted and experimental results are compared in Table 3.

The relative errors of the predicted elastic constants were very small, which verifies the accuracy of the finite element model of plain woven CFRP that included the internal geometric variability.

5 Applications

A finite element analysis was performed to evaluate the performance of the lightweight plain woven CFRP as the

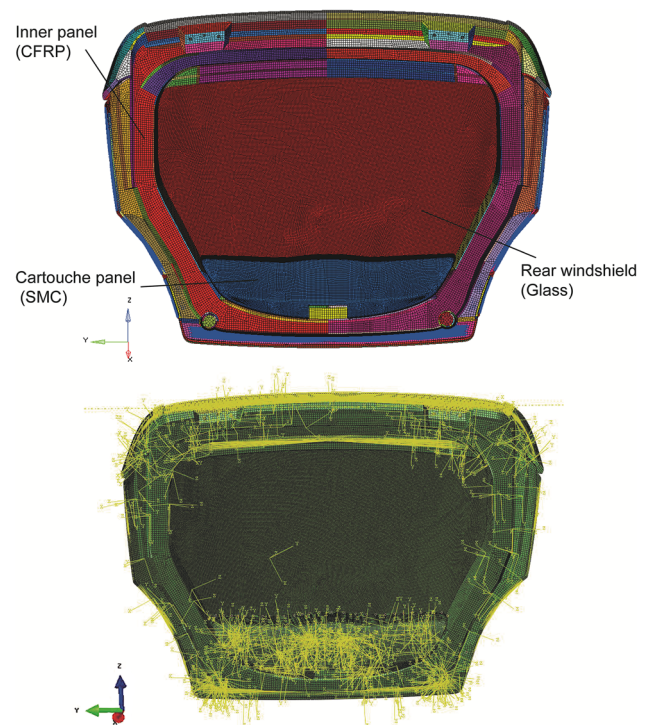


Fig. 8 Finite element model of the back door of an electric car

Table 4 The mechanical properties of the SMC and glass

Properties	Elastic modulus (GPa)	Poisson's ratio
SMC	6.4	0.35
Glass	80	0.25

primary material of a back door of an electric car, which was originally manufactured with an aluminum alloy.

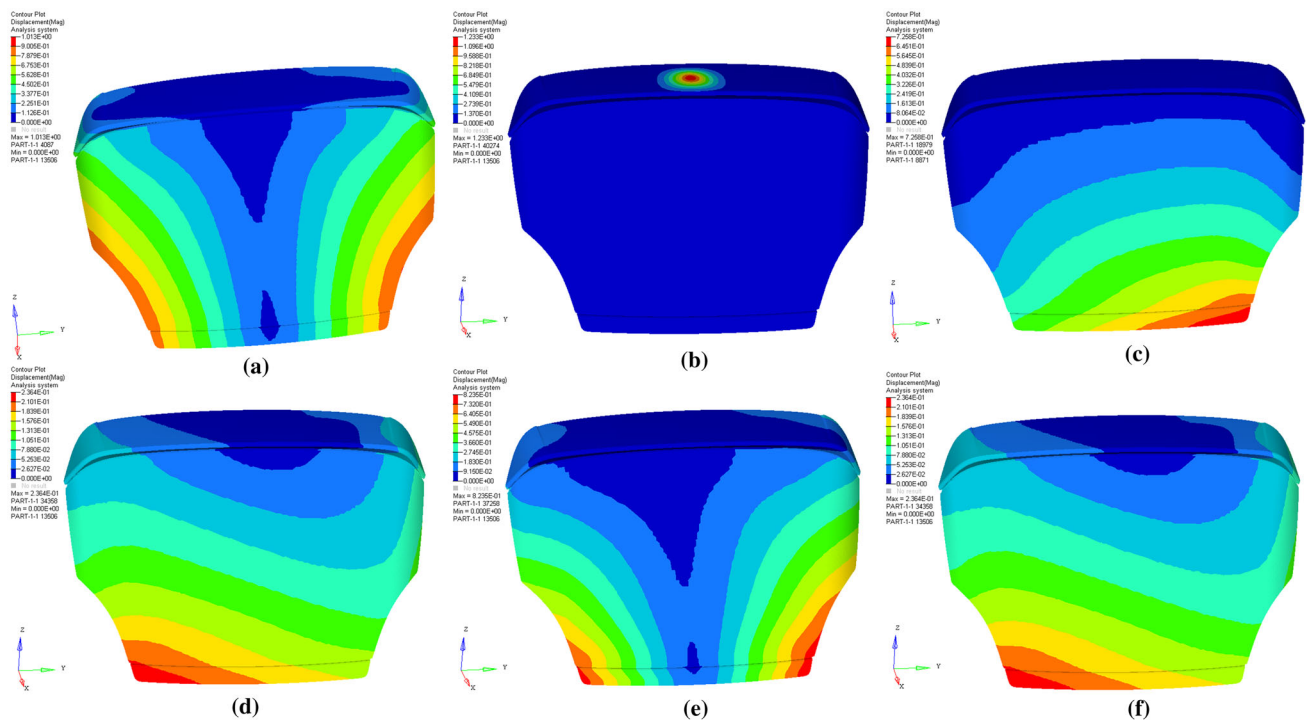


Fig. 9 Displacement contours under different operating conditions: **a** modal, **b** stiffness of the outside panel, **c** lateral stiffness in the closed position, **d** lateral stiffness in the open position, **e** torsional stiffness in the closed position, and **f** torsional stiffness in the open position

Table 5 Performance requirements and responses of the back door under different operating conditions

Operating condition	Performance index	Requirement	Predicted response
Mode constraint	First-order modal frequency	> 30 Hz	68.8 Hz
Stiffness of outside panel	Deformation 1	≤ 7.5 mm	1.233 mm
Lateral stiffness	Deformation 2	≤ 2 mm	1.15 mm
	Deformation 3	≤ 1 mm	0.23 mm
Torsional stiffness	Deformation 4	≤ 1 mm	0.77 mm
	Deformation 5	≤ 1 mm	0.64 mm

The back door shown in Fig. 8 consists of inner and outer panels made of plain woven CFRP, a decorated panel made of a short glass fiber sheet molding compound (SMC), and a glass windshield. The isotropic properties of the SMC and glass are shown in Table 4.

The mechanical properties of the CFRP are illustrated in Table 3. To incorporate the anisotropic material properties of the CFRP, the material model was implemented in Abaqus via UMAT.

The connection between parts was modeled by coupling the assembly at the back door. The finite element model of the back door was divided into several parts according to the shape and spatial position. Considering the anisotropy of the CFRP, local coordinate systems were allocated to each part in the inner panel. In this research, both 0° and 45° were considered in the stacking assignment to balance the mechanical performance. The laminate is assumed to be symmetric with

the stacking sequence as $[0_2/45_2/0_n/45_2/0_2]$. The number of n is adjusted according to the thickness of composite panel.

Four working conditions were investigated to determine the modal properties, stiffness of the outside panel, lateral stiffness, and torsional stiffness of the back door. Figure 9 demonstrates the displacement contours under each condition. Detailed performance requirements and corresponding responses are given in Table 5. “Deformation 1” for the stiffness of the outside panel is the deformation after applying a 220-N force. For the lateral stiffness, “Deformation 2” is the deformation after applying 180 N in the closing direction on the side away from the strut while the tailgate is in the open position, and “Deformation 3” is the deformation after applying 120 N in the direction of the parallel hinge axis while the tailgate is in the closed position. For torsional stiffness, “Deformation 4” and “Deformation 5” represent the deformations after applying opposite forces of 240 N on the two corners while the tailgate is in the closed position and

after applying opposite forces of 220 N on the two corners while the tailgate is in the open position, respectively.

As shown in Table 5, all performances met the design requirements, and the thickness of the inner panel was reduced from 3 to 2.5 mm. After the structure was redesigned to facilitate the use of CFRP, the mass of the inner panel was 2.086 kg, which was 59.63% lighter than the original structure. The weight of the total back door system was reduced by 47.45%. Moreover, most performance responses were far better than the requirements, which further indicates the potential of using lightweight structures made of CFRP in vehicles.

6 Conclusions

In this work, the variability of the internal geometry of plain woven CFRP was modeled with the proposed reconstruction algorithm and the elastic properties were calculated by finite element analysis.

First, the real architecture of plain woven CFRP was measured with a micro-CT method, from which the geometric parameters were extracted. A statistical analysis of the mean and standard deviation of the parameters and the correlation characteristics was conducted to quantify the geometry.

Second, an algorithm using CGRS was investigated to generate geometric parameters that were statistically equivalent to the measured values. The geometric model was established from the reconstructed parameters, which was close to the real structure of the studied composite. As can be observed from the modeling and simulation results, the proposed reconstruction method could effectively build the statistical equivalent structures of RVE and elastic properties of plain woven CFRP could be accurately predicted using homogenous approach based on established RVE geometry and finite element method. A finite element model of the RVE based on homogenization theory was built to calculate the elastic constants of the CFRP. Comparison between experimental and predicted values showed the accuracy of the developed method, which also indirectly verified the effectiveness of the proposed reconstruction algorithm.

Finally, CFRP was used in the back door of an electric vehicle to achieve a lightweight design. The stiffness and modes of the back door made of the composite were calculated. Good working performance of the CFRP back door was demonstrated. CFRP has shown excellent advantages in perspective of lightweight in automotive structures. However, design optimization can be further studied to achieve an even lighter weight, which will be considered in future work.

Acknowledgements This work was supported by the National Natural Science Foundation of China (Grant Nos. 11372181, 11772191, 51705312) and the China Postdoctoral Science Foundation (Grant

No. 2017M61156). The authors acknowledge the support provided by Shanghai Jiao Tong University to Prof. Wei Chen.

References

1. Lee, J.M., Lee, K.H., Kim, B.M., et al.: Design of roof panel with required bending stiffness using CFRP laminates. *Int. J. Precis. Eng. Manuf.* **17**(4), 479–485 (2016)
2. Sequeira, G.J., Lugner, R., Steinhauser, D., et al.: Investigation of intelligent features for CFRP structure in automotive safety systems. In: 2017 2nd IEEE International Conference on Intelligent Transportation Engineering (ICITE), Singapore, pp. 18–24 (2017)
3. Fuchs, E., Field, F., Roth, R., et al.: Strategic materials selection in the automobile body: economic opportunities for polymer composite design. *Compos. Sci. Technol.* **68**(9), 1989–2002 (2008)
4. Liu, Q., Lin, Y., Zong, Z., et al.: Lightweight design of carbon twill weave fabric composite body structure for electric vehicle. *Compos. Struct.* **97**, 231–238 (2013)
5. Obert, E., Daghia, F., Ladevèze, P., et al.: Micro and meso modeling of woven composites: transverse cracking kinetics and homogenization. *Compos. Struct.* **117**, 212–221 (2014)
6. Gao, J., Liang, B., Zhang, W., et al.: Multiscale modeling of carbon fiber reinforced polymer (CFRP) for integrated computational materials engineering process. In: Purdue University, Proceedings of the American Society for Composites—Thirty-second Technical Conference, Indiana, USA (2017)
7. Mesogitis, T.S., Skordos, A.A., Long, A.C.: Uncertainty in the manufacturing of fibrous thermosetting composites: a review. *Compos. Part A Appl. Sci. Manuf.* **57**, 67–75 (2014)
8. Komeili, M., Milani, A.S.: The effect of meso-level uncertainties on the mechanical response of woven fabric composites under axial loading. *Comput. Struct.* **90**, 163–171 (2012)
9. Zhou, X.Y., Gosling, P.D.: Influence of stochastic variations in manufacturing defects on the mechanical performance of textile composites. *Compos. Struct.* **194**, 226–239 (2018)
10. Lee, S.-K., Byun, J.-H., Hong, S.H.: Effect of fiber geometry on the elastic constants of the plain woven fabric reinforced aluminum matrix composites. *Mater. Sci. Eng. A* **347**(1), 346–358 (2003)
11. Endruweit, A., Long, A.C., Robitaille, F., et al.: Influence of stochastic fibre angle variations on the permeability of bi-directional textile fabrics. *Compos. Part A Appl. Sci. Manuf.* **37**(1), 122–132 (2006)
12. De Carvalho, N.V., Pinho, S.T., Robinson, P.: An experimental study of failure initiation and propagation in 2D woven composites under compression. *Compos. Sci. Technol.* **71**(10), 1316–1325 (2011)
13. Goldsmith, M.B., Sankar, B.V., Haftka, R.T., et al.: Effects of microstructural variability on thermo-mechanical properties of a woven ceramic matrix composite. *J. Compos. Mater.* **49**(3), 335–350 (2015)
14. Olave, M., Vanaerschot, A., Lomov, S.V., et al.: Internal geometry variability of two woven composites and related variability of the stiffness. *Polym. Compos.* **33**(8), 1335–1350 (2012)
15. Desplentere, F., Lomov, S.V., Woerdeman, D.L., et al.: Micro-CT characterization of variability in 3D textile architecture. *Compos. Sci. Technol.* **65**(13), 1920–1930 (2005)
16. Barbero, E.J., Trovillion, J., Mayugo, J.A., et al.: Finite element modeling of plain weave fabrics from photomicrograph measurements. *Compos. Struct.* **73**(1), 41–52 (2006)
17. Bale, H., Blacklock, M., Begley, M.R., et al.: Characterizing three-dimensional textile ceramic composites using synchrotron X-ray micro-computed-tomography. *J. Am. Ceram. Soc.* **95**(1), 392–402 (2012)

18. Vanaerschot, A., Cox, B.N., Lomov, S.V., et al.: Stochastic framework for quantifying the geometrical variability of laminated textile composites using micro-computed tomography. *Compos. Part A Appl. Sci. Manuf.* **44**, 122–131 (2013)
19. Blacklock, M., Bale, H., Begley, M., et al.: Generating virtual textile composite specimens using statistical data from micro-computed tomography: 1D tow representations for the Binary model. *J. Mech. Phys. Solids* **60**(3), 451–470 (2012)
20. Rinaldi, R.G., Blacklock, M., Bale, H., et al.: Generating virtual textile composite specimens using statistical data from micro-computed tomography: 3D tow representations. *J. Mech. Phys. Solids* **60**(8), 1561–1581(2012)
21. Stock, S.R.: Recent advances in X-ray microtomography applied to materials. *Int. Mater. Rev.* **53**(3), 129–181 (2013)
22. Xia, Z., Zhang, Y., Ellyin, F.: A unified periodical boundary conditions for representative volume elements of composites and applications. *Int. J. Solids Struct.* **40**(8), 1907–1921 (2003)